Journal of Materials Chemistry A

PAPER

View Article Online
View Journal | View Issue

Cite this: J. Mater. Chem. A, 2015, 3, 11320

Dye-sensitized solar cells based on hierarchically structured porous TiO_2 filled with nanoparticles†

Zhenxuan Zhao,[a] Guicheng Liu,[a] Bo Li,[b] Lixue Guo,[a] Chengbin Fei,[a] Yajie Wang,[a] Lili Lv,[b] Xiaoguang Liu,[b] Jianjun Tian[ab] and Guozhong Cao*[ac]

Received 17th March 2015
Accepted 13th April 2015

DOI: 10.1039/c5ta01953b

www.rsc.org/MaterialsA

A new morphology of TiO_2 photoanodes for N-719 dye-sensitized solar cells (DSCs) has been developed with enhanced power conversion performance. Strategies for the synthesis of hierarchically structured three-dimensionally ordered macroporous (HS-3DOM) TiO_2 with controlled macropore sizes (*ca.* 85–155 nm) by using well-arrayed polymethyl methacrylate with different diameters as well as two kinds of photoanode films based on hierarchically structured porous TiO_2 filled with nanoparticles have been demonstrated. DSCs based on a special TiO_2 photoanode with a macropore size of 105 nm exhibited a current density (J_{sc}) of 20.6 mA cm^{-2} and a high photo-to-electrical energy conversion efficiency (η) of 9.7%. This high power conversion efficiency is ascribed to the special morphology of the TiO_2 photoanode with high dye adsorption due to its ordered and open structures, and also its light scattering and charge collection efficiency.

1. Introduction

The utilization of solar energy becomes increasingly important, as the fossil and mineral sources are limited and also the main sources of environmental pollution. Dye-sensitized solar cells (DSCs) based on nanostructured semiconductor films as a type of photovoltaic device have been considered as promising alternatives to silicon-based solar cells due to their low cost of materials and manufacturing.[1] However, improving their relatively low power conversion efficiency remains a big challenge confronting us because of the highest efficiency of up to 13% compared with ~20% of silicon-based solar cells.[2] A photoelectrode, when loaded with dyes, as a component of DSCs is important due to its role as a light harvester, charge generator, as well as an electron collector.[3] The pore size, specific surface area, surface chemistry and defects, charge mobility, and charge recombination at the interface are all critical in achieving high power conversion efficiency.[1d,4] Therefore, a lot of research including fabrication of semiconductors with desired and unique micro and nanostructures as photoelectrodes, most commonly TiO_2 and ZnO_2, has been carried out to enhance the power conversion efficiency of DSCs.

In comparison with the bulk material, nanocrystalline photoelectrodes can adsorb more dye molecules due to their high specific surface area.[5] However, the existence of numerous boundaries in nanocrystalline films would unavoidably increase their interfacial charge recombination and reduce the charge mobility. Nanowires, nanorods, or nanotubes with one-dimensional structures in single crystal form would provide direct pathways for efficient electron transport to reduce charge recombination at the interface or grain boundaries;[3a,6] however, one dimensional nanostructures suffer from a relatively low specific surface area to ensure sufficient dye loading. Photoelectrodes with hierarchical structures exhibit many advantages in enhancing the power conversion efficiency of DCSs,[7] such as possessing a large specific surface area and effective light scattering, accommodating sufficient dye loading, facilitating electron transport and electrolyte diffusion due to the compact packing of the nanocrystallites and the relatively open structure.[4] Hierarchical structures, which have been studied in the field of DSCs, include spherical/nanorod/core–shell aggregates.[7a,c,8]

Three-dimensionally ordered macroporous (3DOM) TiO_2 has attracted particular attention in photocatalytic[9] and photovoltaic[10] applications due to its high surface area, novel optical and electronic abilities, interconnected porosity, extremely uniform size, and periodic distributions of pores. 3DOM TiO_2 can be fabricated by using monodisperse latex spheres as a hard template.[11] However, the overlayers on top of the 3DOM architecture destroy the quality of 3DOM TiO_2 due to the air- and moisture-sensitivity of titanium alkoxides. Therefore many synthetic methods such as a sandwich-vacuum method[12] and an opal infiltration method[13] by using polystyrene as a template

[a]Beijing Institute of Nanoenergy and Nanosystems, Chinese Academy of Sciences, Beijing 100083, P. R. China. E-mail: gzcao@u.washington.edu

[b]Advanced Material and Technology Institute, University of Science and Technology, Beijing 100083, P. R. China

[c]Department of Materials and Engineering, University of Washington, Seattle, WA98195-2120, USA

† Electronic supplementary information (ESI) available. See DOI: 10.1039/c5ta01953b

have been adopted. Herein, a simple method using self-assembled polymethyl methacrylate (PMMA) spheres as templates and tetraisopropyl titanate solution with moisture stability was used to fabricate high quality hieratically structured 3DOM TiO_2 under ambient conditions. After the removal of PMMA spheres and subsequent heat treatment, a kind of hierarchically structured porous TiO_2 filled with nanoparticles has been studied as the photoanode in DSCs and the impacts of such hierarchical structures on dye loading, light scattering and charge transport properties, and the consequent power conversion efficiency have been studied and discussed.

2. Results and discussion

Fig. 1(a–e) show the SEM images of the as-fabricated hierarchically structured three-dimensionally ordered macroporous TiO_2 after the removal of PMMA templates. All of these samples exhibited excellent three-dimensionally ordered macroporous architectures. It indicates that TiO_2 with three-dimensionally ordered macroporous structures could be successfully fabricated with regularly packed PMMA microspheres, and their qualities were better than that of three-dimensionally quasi-ordered macropore TiO_2 prepared through a poly(vinyl alcohol) gelated crystalline colloidal array.[14] We synthesized four samples with macropore diameters of *ca.* 155, 115, 105, and 85 nm. In Fig. 1(f), the positions of XRD lines for all the samples were the same and could be well indexed to the standard anatase TiO_2 XRD pattern (JCPDS PDF no. 78-2486). Therefore, it can be deduced that all these samples possessed an anatase crystal structure.[15] It has been reported that the macropore diameters could be controlled by the size of the PMMA microspheres.[16] The SEM images of hard templates shown in Fig. S1 of ESI† exhibited the well-arrayed PMMA microsphere templates with 280, 220, 200, and 150 nm diameter and their

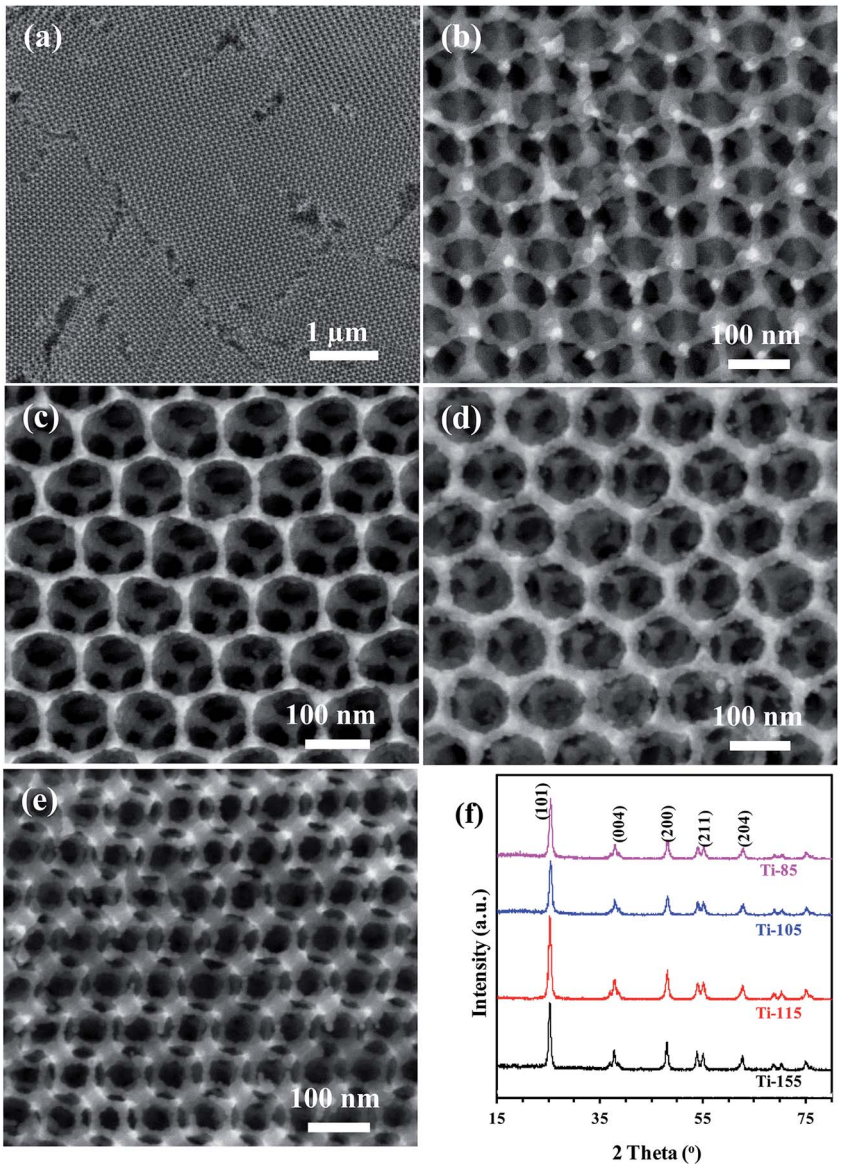

Fig. 1 (a–e) SEM images of HS-3DOM TiO_2 samples: (a and b) Ti-155, (c) Ti-115, (d) Ti-105, and (e) Ti-85, as well as (f) their XRD patterns.

corresponding pore sizes in TiO_2 samples are 155, 115, 105, and 85 nm, respectively. The size of the macropore in 3DOM TiO_2 samples is 55% smaller than the diameter of PMMA microspheres. It can be easily understood that after the removal of the PMMA microsphere through decomposition and oxidation during thermal treatment, loosely assembled TiO_2 nanoparticles would go through slight adjustment and partial sintering and densification leading to the shrinkage of void spaces. What is more, the surfaces of all these 3DOM TiO_2 samples were rough as observed from SEM images (Fig. 1(a–e)). Under TEM observation (Fig. 2), detailed morphological structures can be seen and that the frameworks of these TiO_2 samples with 3DOM architectures were comprised of nanoparticles of 7–35 nm. The high-resolution TEM (HR-TEM) image in Fig. 2(f) shows that the lattice space (d) of nanoparticles was 0.35 nm and matches nearly exactly to the theoretical value (3.5165 Å) of the (101) plane of crystalline anatase TiO_2.

The nitrogen adsorption–desorption isotherms of the TiO_2 samples are shown in Fig. S2(A).† According to the IUPAC classification, the adsorption isotherms can be classified as type II isotherms.[17] An adsorption–desorption hysteresis loop with a H3 type is observed in the relative pressure (p/p_0) range of 0.8–1.0,[17a] which does not clearly exhibit any adsorption plateau at relative pressures close to saturation, suggesting the fact of macropore existence,[17a] which was identical to the macroporous structures observed from the SEM images. What is more, the low-pressure portion of the almost linear middle section of the isotherm, which is attributable to the unrestricted mono- or multilayer adsorption, indicates the existence of macropores.[18]

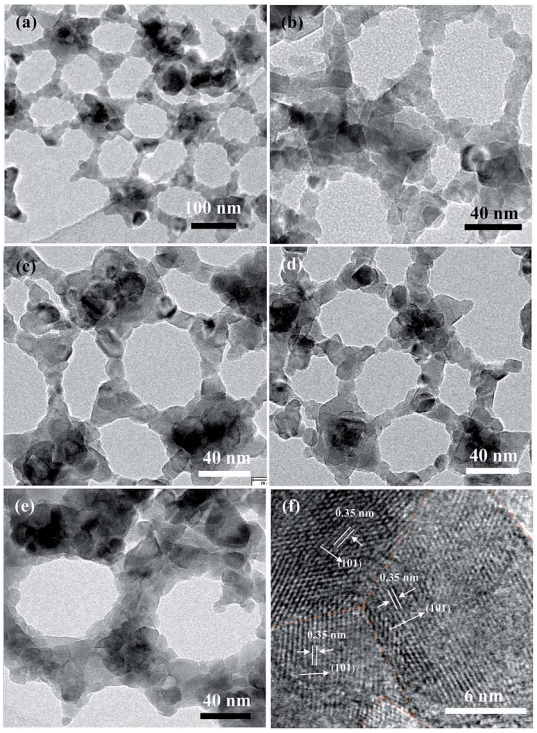

Fig. 2 TEM images of (a and b) Ti-155, (c) Ti-115, (d) Ti-115, (e) Ti-85 samples and the HR-TEM image shows d-spacing of the HS-3DOM TiO_2.

Furthermore, there are initial jumps of adsorption isotherms observed from the low-pressure section in Fig. S2(C).† It represents the existence of micropores.[19] The pore size distribution curves calculated by the BJH method are shown in Fig. S2(B).† All samples exhibited two pore size distributions: one broad peak centered at 29–45 nm and one narrow peak centered at 2–10 nm and, which can be due to the macropores generated by the removal of PMMA spheres and micropores which are the gaps between adjacent packed nanoparticles, respectively. This result was in good agreement with that of adsorption–desorption isotherms and the observation from TEM images. Table S1† lists their BET surface areas and pore volumes. It was found that the surface areas and pore volumes increased in the range of 46.1–114.5 $m^2\ g^{-1}$ and 0.25–0.82 $cm^3\ g^{-1}$, respectively, with the decreasing macropore size of HS-3DOM TiO_2 samples from 155 nm to 85 nm. In contrast, a decline trend was observed in the values of the surface area/pore volume from 184 cm^{-1} to 140 cm^{-1} while the macropore sizes were decreased.

The pastes based on HS-3DOM TiO_2 were obtained by the treatments described in the Experimental section. The cross-sectional SEM images of the photoanode based on Ti-155 are shown in Fig. 3(a), the thickness of the porous TiO_2 layer was about 9 μm and the compact layer, which was used as a hole-blocking layer to prevent the direct contact between the FTO and electrolyte, was about 0.3 μm. A configuration of a full DSC-device is illustrated in Fig. 3(b). From magnifying images of the Ti-155 layer shown in Fig. 3(c and d), it can be observed that HS-3DOM TiO_2 particles had been broken into small particles. However, they did not lose their three-dimensionally ordered skeletal structure completely. These splitting particles mixed together randomly to form a disordered status. From the images of the Ti-85 layer in Fig. 3(f and g), it can be found that many nanoparticles were covered on the surface of particles with 3DOM structures. The status was different from the former one. We deduced that small particles with 3DOM architectures and nanoparticles, which can be broken from their mother particles easily, could generate after the same experimental treatments in all samples. As for the Ti-155 paste, some nanoparticles could be filled into macropores as described in Fig. 3(e). So, it is hard to find nanoparticles from the SEM image of the Ti-155 layer in Fig. 3(d). Whereas, as for the Ti-85 pastes, macropores with a smaller size could not allow the nanoparticles to enter, they have to stay out of the pores as illustrated in Fig. 3(h). There are many factors for these two kinds of special morphology pastes that facilitate the performance of DSCs. For one thing, as depicted in the schemes (Fig. 3(e and h)), lots of nanocrystallites broken from larger particles can help contribute to enhancing their surface area which adsorbed N719 dye for light harvesting. Secondly, the ordered structure is beneficial to photogenerated charge transportation as shown in Fig. 3(e). Lastly, the porous TiO_2 possesses a relatively open structure which allows the I^-/I_3^- electrolyte to completely wet its surface and facilitate electrolyte diffusion.

A strategy for preparing HS-3DOM TiO_2 with tunable macropore sizes has been developed by using a crystalline colloidal array PMMA photonic crystal microsphere packed in the form of the face-centered-cubic structure as a template shown in

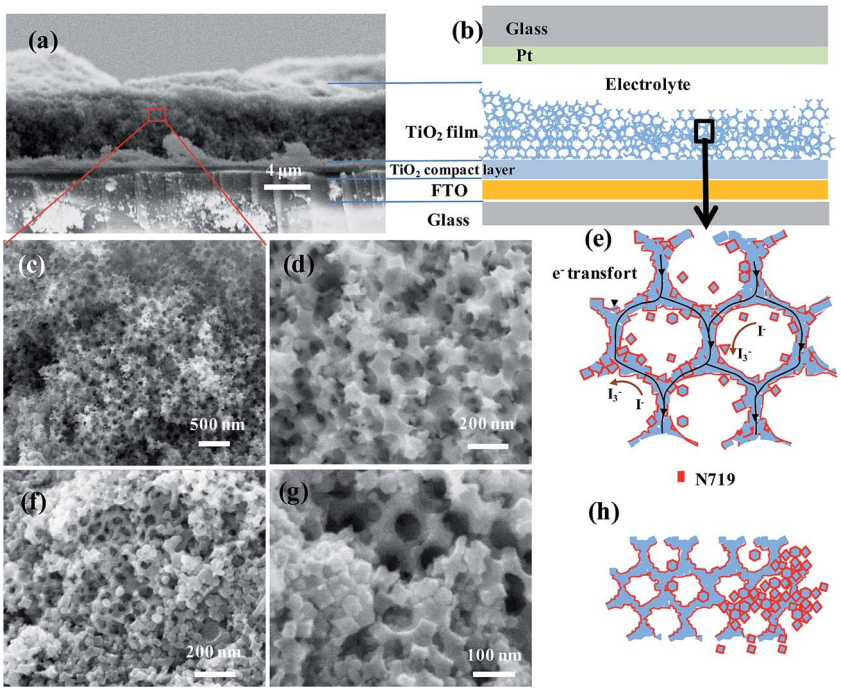

Fig. 3 (a) Cross-sectional SEM image of the Ti-155 film without dye loading, (b) configuration of a full DSC-device based on HS-3DOM TiO_2 in this study, high-resolution SEM images of (c and d) T-155, (f and g) Ti-85 layers and their structural illustrations of T-155 (e) and Ti-85 (h) layers.

Fig. 4(a) and tetraisopropyl titanate with PEG-400 and HNO_3 in EtOH solution as a Ti precursor. The first step was dipping the well-arrayed PMMA powder (Fig. 4(a)) into the Ti precursor solution for four hours. Then, the residual solution has been removed and the remaining solution has been absorbed into the voids of the hard template by the force of capillary pressure as described in Fig. 4(b). EtOH or absorbing water from air can be removed through drying at ambient temperature and calcination at 160 °C for 3 h, which was confirmed by the TGA/DSC measurement (Fig. S3 in ESI†). Then, the micelle will rearrange during the removal of EtOH solution due to the density of the micro-emulsion reaching the critical density as shown in Fig. 4(c). In this state, the organic molecule (PEG-400, $(CH_3)_2CHO$) becomes an inhibiter to wrap up Ti compounds, which was mainly $TiO(OH)_2$ as described in Fig. 4(c). After calcination at 550 °C in an air atmosphere, organic molecules

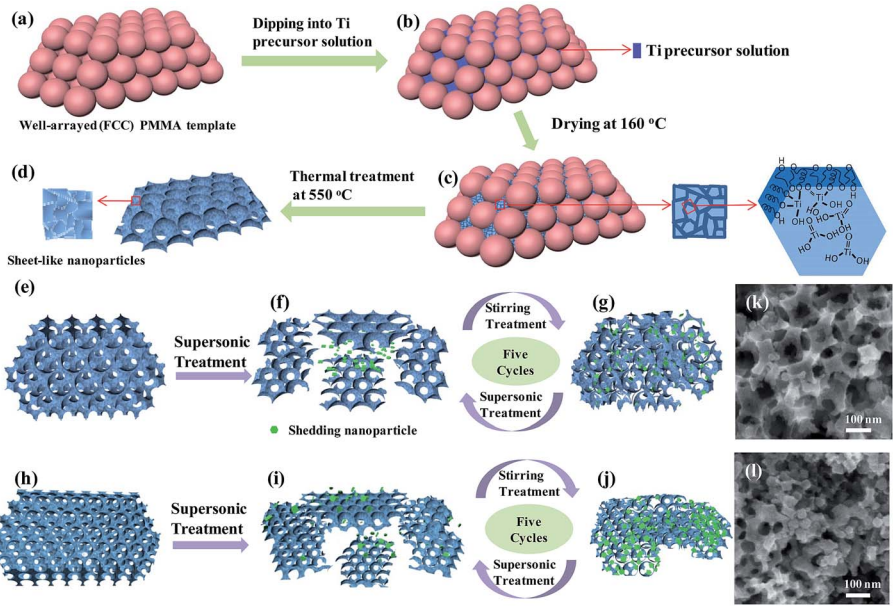

Fig. 4 Schematic illustration of the paste formation process based on (a) Ti-155, Ti-155, and Ti-105 samples and the ones based on (c) Ti-85 sample, as well as HR-SEM pictures of photoanode films based on (k) Ti-105 and (l) Ti-85 samples.

including PEG-400, $(CH_3)_2CHO$, and PMMA were removed thoroughly, and $TiO(OH)_2$ was decomposed and turned into anatase TiO_2 with HS-3DOM structure aggregated nanoparticles shown in Fig. 4(d). According to different macropore sizes of HS-3DOM TiO_2, the hierarchically structured porous TiO_2 layers present two kinds of morphologies as shown in the HR-SEM images (Fig. 4(k and l)). Their big particles could break into many pieces when subjected to ultrasonication and still maintain 3DOM architectures (Fig. 4(f and i)). As for the Ti-155, Ti-115, and Ti-105 pastes with macropore sizes larger than 105 nm (Fig. 4(e)), big particles blend together randomly and split nanoparticles could get into the macropores of big pieces, which were large enough to let these nanoparticles fall into them (Fig. 4(g)). As for the Ti-85 pastes, most nanoparticles were blocked at the surface of macroporous particles due to their smaller macropore size as observed in Fig. 4(i).

Fig. 5 shows the current density–voltage (J–V) curves of DSCs based on hierarchically structured porous TiO_2 filled with nanoparticles. The power conversion efficiency of these devices increased from 7.08% to 9.74% along with the decreasing macropore size of porous TiO_2 layers from 155 nm to 105 nm as listed in the table inserted in Fig. 5. In particular, the solar cell device based on Ti-105 exhibited a short-circuit current density (J_{sc}) of 20.68 mA cm^{-2} and an energy conversion efficiency (η) of 9.74%. Compared to the DSC device based on the Ti-105 film, devices based on Ti-155 and Ti-115 had J_{sc} and η values of 16.35 mA cm^{-2}, 7.07%, and 19.92 mA cm^{-2}, 8.17%, respectively, with the lowest power conversion efficiency of 6.15% found in DSCs based on the Ti-85 film. Their open-circuit voltages V_{oc} (718 ± 11 mV) determined by the difference between the Fermi levels of the oxide semiconductor and the redox potential of the electrolyte were almost the same in all of the hierarchically structured porous TiO_2 devices.[20] Their fill factors FF, which were imitated with the geometry structure and the transport mechanism of carriers in each individual cell,[20] varied from 57.9% to 64.9%.

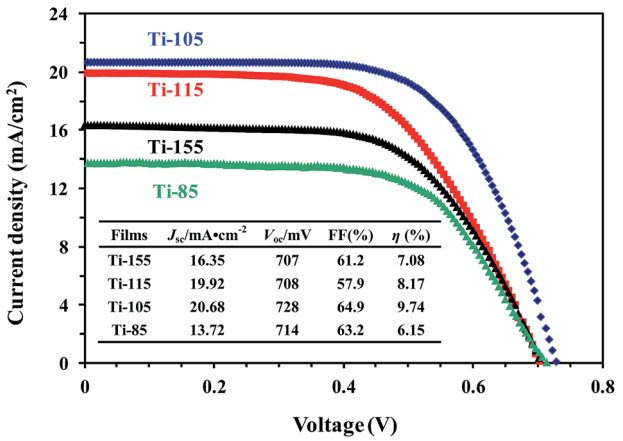

Films	J_{sc}/mA•cm^{-2}	V_{oc}/mV	FF(%)	η (%)
Ti-155	16.35	707	61.2	7.08
Ti-115	19.92	708	57.9	8.17
Ti-105	20.68	728	64.9	9.74
Ti-85	13.72	714	63.2	6.15

Fig. 5 J–V curves of DSC devices based on HS-3DOM TiO_2 with different macropore sizes and parameters of the photovoltaic performance of DSCs devices based on three-dimensionally ordered hierarchically porous TiO_2 (inset).

The amount of adsorbed dye on each cell was investigated; Table 1 shows that the amounts of adsorbed dye on hierarchically structured porous TiO_2 increased from 238 nmol cm^{-2} to 264 nmol cm^{-2} with reduced macropore sizes in Ti-155, Ti-115, and Ti-105 photoanodes, and dropped dramatically to 233 nmol cm^{-2} on the Ti-85 one. In order to investigate the amount of dye adsorption which was altered with the changing macropore sizes in our synthesized photoanode films, the surface area and pore volume of all powders obtained from drying pastes, which were used to assemble as photoanodes, had been detected by nitrogen sorption isotherms and calculated by BET and BJH methods, respectively. Observed from the texture parameters listed in Table 1, the values of the surface area became larger than those of their corresponding samples before treatment (Table S1†). The total area per square centimeter of photoanode A can be deduced by the value of the surface area (a) and pore volume (v_p). A given volume v of per gram porous material includes the volume of 1 g bulk material and the total one of pores in 1 g porous material, just as the pore volume (v_p), can be calculated as eqn (1):

$$v(\mathrm{cm}^3) = \frac{1}{\rho_{\mathrm{bulk}}} + v_p = 0.257 + v_p \quad (1)$$

where $\rho_{bulk} = 3.893\ \mathrm{cm}^3\ \mathrm{g}^{-1}$ is the density of bulk anatase TiO_2. Therefore, the total surface area per square centimeter of photoanode A can be calculated by the following eqn (2).

$$A(\mathrm{cm}^2) = V\rho a = \frac{9.5 \times 10^{-4} a}{0.257 + v_p} \quad (2)$$

where d is the thickness of the photoanode film. It was about 9.5 μm in our photoanodes. All of the data are listed in Table 1. The resulting value of A increased in the range of Ti-155 < Ti-115 < Ti-105 from 1.076×10^{17} nm^2 to 1.143×10^{17} nm^2 and dropped to 1.045×10^{17} nm^2 in the Ti-85 sample. It has been reported that per 1 nm^2 TiO_2 can be filled with 1.95 N719 molecules.[1a] Therefore, we can calculate that the ideal amount of adsorbed dye in 1 cm^2 active area of devices varied from 338.6 to 358.8 nmol cm^{-2} and is listed in Table 1. Apparently, the amount of adsorbed dye was *ca.* 70% of ideal ones and has the same sequence with their J_{sc} values, which were higher than that (7–10 mA cm^{-2}) of DSCs based on TiO_2 nanoparticles with the same dye coverage.[1a] Furthermore, the as-assembled solar cell based on Ti-105 with 264 nmmol cm^{-2} dye-loading performed much better than the one based on the three-dimensional array of TiO_2 nanotubes with nearly the same amount of adsorbed dye (260 nmmol cm^{-2}).[21]

Diffused reflectance and transmittance of hierarchically structured porous TiO_2 layers with and without dye adsorption were measured using a UV-vis spectrophotometer to characterize their light scattering, which is an important factor influencing the performance of DSCs. It is widely known that the ideal light scattering activities of the photoanode should have a higher diffuse reflectance and lower diffuse transmittance. In Fig. 6(A and B), the diffuse reflectance of the bare porous TiO_2 layer was in the sequence of Ti-155 < Ti-115 < Ti-105 in the range of 400–800 nm, corresponding to their transmission in the order of Ti-155 > Ti-115 > Ti-105. The increased reflectance and

Table 1 Texture parameters of the as-fabricated photoanodes and their amount of adsorbed dye

Device based on	a (m^2 g^{-1})	v_p (cm^3 g^{-1})	ρ/g cm^{-3}	A ($\times 10^{17}$ nm^2)	Ideal amount of adsorbed dye (nmol cm^{-2})	Amount of adsorbed dye (nmol cm^{-2})
Ti-155	56.3	0.24	2.01	1.076	348.6	238
Ti-115	66.6	0.32	1.73	1.096	355.2	250
Ti-105	83.6	0.46	1.39	1.107	358.8	264
Ti-85	109.7	0.74	1.00	1.045	338.6	233

suppressed transmission along with the decreasing macropore sizes in Ti-155, Ti-115, and Ti-105 films may be ascribable to sufficient light scattering due to their porous architectures.[22] However, it is interesting that the reflectance of Ti-85 did not continue to increase with decreasing macropore size and became weaker than that of Ti-155 in the range of 500–800 nm. This result may be ascribable to their morphologies. Furthermore, the diffused reflectance and transmission of dye-adsorbed porous TiO_2 films have been investigated and are shown in Fig. 6(C and D). Apparently, they have the same sequences in the reflectance and transmission abilities in the dye-absorbed porous TiO_2 layer according to their corresponding layers without dye loading.

The transport and interfacial transfer of electrons in DSCs can be investigated using intensity modulated photocurrent and photovoltage spectroscopy (IMPS/IMVS). The effective electron transport (τ_t) and electron lifetime (τ_r) can be obtained from IMPS/IMVS measurements by adjusting the light intensity to determine the open-circuit voltage, respectively. The data can be calculated using eqn (3) and (4) shown below:[23]

$$\tau_t = 1/2\pi f_t \quad (3)$$

$$\tau_r = 1/2\pi f_r \quad (4)$$

where f_t and f_r are the characteristic frequency minima of the IMPS and IMVS imaginary components, respectively. Fig. 7(A

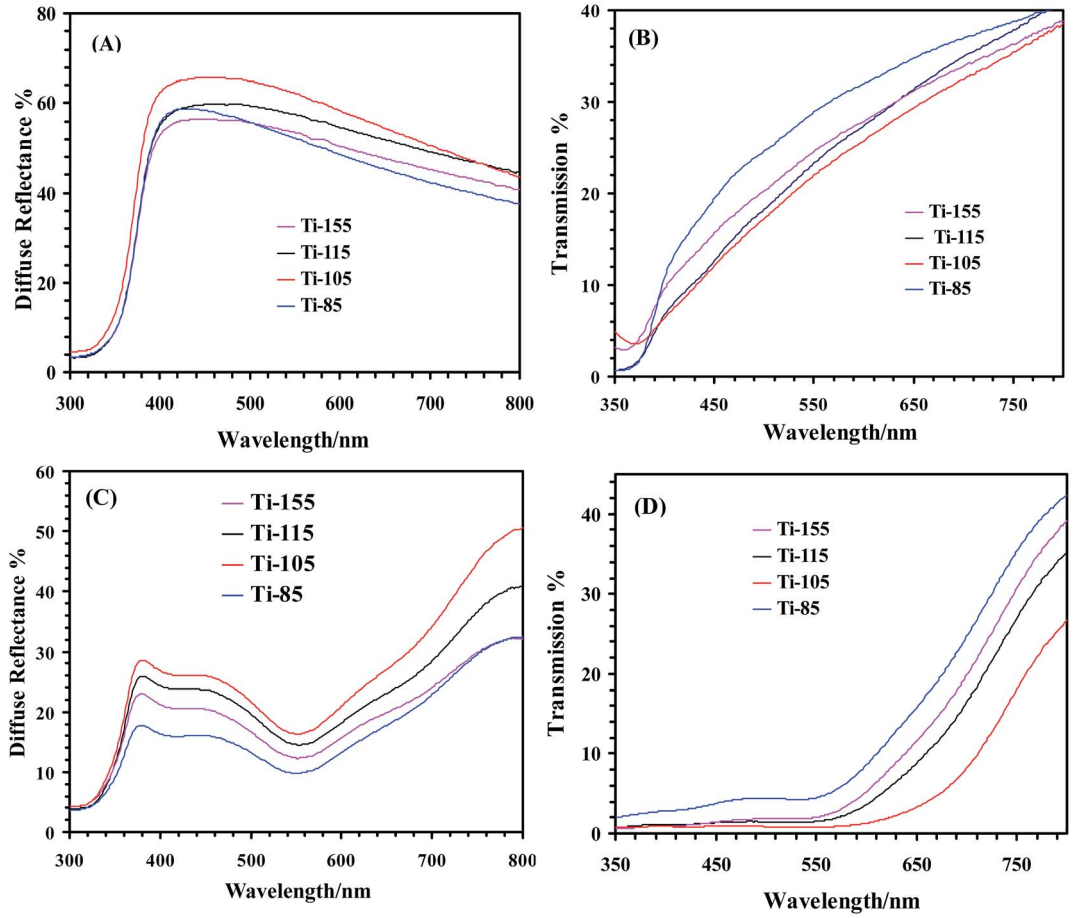

Fig. 6 (A and C) Diffuse reflectance and (B and D) transmittance of porous TiO_2 layers based on HS-3DOM TiO_2 (A and B) without and (C and D) with N-719 sensitization.

and B) show the τ_t and τ_r plots as a function of open-circuit voltage for DSCs based on Ti-155, Ti-115, Ti-105, and Ti-85. Obviously, the τ_t of all devices was decreasing slowly with the increasing voltage, which can be attributed to the trapping/detrapping of electrons with shallower levels due to the deep traps filled by more photoelectrons at higher voltage. As for the τ_r, the decrease is ascribable to the increase in the electron recombination rate in higher voltage. Furthermore, the τ_t and τ_r of these DSCs were increasing slightly in the sequence of Ti-155 < Ti-115 < Ti-105 < Ti-85, suggesting that the electron transport rate and electron recombination rate decreased a little with the increasing macropore size in hierarchically structured porous TiO_2. It is said that the electron recombination could enhance with the increasing surface area/pore volume due to the increasing surface defects that result in more charge trapping.[24] However, the electron recombination rate of DSCs based on Ti-85 which possessed the largest surface area/pore volume (140 cm^{-1}) listed in Table S1† was the lowest compared to other devices. This maybe due to the special geometry architecture of the photoelectrodes. Furthermore, the electron collection efficiency (η_{col}) can be estimated using τ_t and τ_r according to eqn (5) given below:[25]

$$\eta_{col} = \frac{J_{sc}}{J_{inj}} = \frac{J_{sc}}{J_{sc} + J_r} = \frac{\frac{1}{\tau_t}}{\frac{1}{\tau_t} + \frac{1}{\tau_r}} = 1 - \frac{\tau_t}{\tau_r} \quad (5)$$

where J_{inj} is the electron-injection current density from the excited dye to TiO_2 and J_r is the recombination-current density. Fig. 7(C) shows the η_{col} plots as a function of voltage from 0.18 V to 0.90 V. The η_{col} of the DSCs increased in the order of Ti-85 < Ti-155 < Ti-115< Ti-105 with the same range of J_{sc} which is proportional to η_{col} as depicted in eqn (5).

The electrochemical impedance spectroscopy (EIS) analysis was carried out to study the charge-transfer properties in the DSCs based on hierarchically structured porous TiO_2 as photoelectrodes; the Nyquist plots of the EIS results including various resistance elements for these DSC devices are shown in Fig. 7(D) and Table 2. The equivalent circuit can be interpreted by resistance–capacitance elements inserted in Fig. 7(D). The impedance plots of a DSC device have two semicircles in the Nyquist diagram as shown in Fig. 7(D). The first semicircle at high frequencies (R_t) is generated by the redox reaction at the platinum counter electrode/electrolyte interface; another one at lower frequencies (R_{ct}) can be ascribable to the electron transfer between the oxide/electrolyte interface and is equivalent to the recombination resistance;[26] the ohmic resistance R_s is caused by the sheet resistance of the FTO glass.[8] It is obvious that R_s and R_t of the DSCs were almost 6.92 and 2.45 Ω cm^2, respectively, and the extent of the numerical value variation was very small; the R_{ct} of all DSCs based on hierarchically structured porous TiO_2 increased from 10.97 to 16.55 Ω cm^2 with the decreasing macropore size of photoelectrodes. It means that the ohmic resistance and the redox reaction resistance at the counter electrode of these DSCs were almost equal; the charge recombination

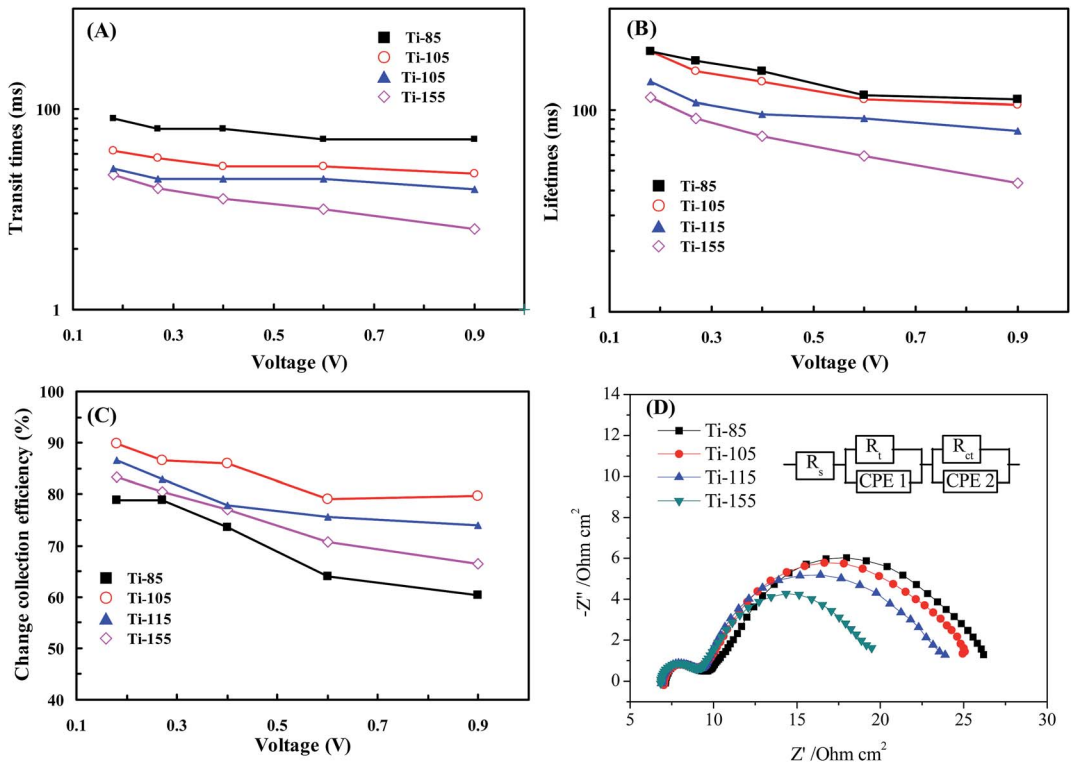

Fig. 7 (A) Electron transit times and (B) electron lifetime, (C) the charge collection efficiency measured by intensity-modulated photocurrent/photovoltage spectroscopy (IMPS/IMVS) for cells based on Ti-155, Ti-115, Ti-105, and Ti-85, and (D) Nyquist plots of N719 dye-sensitized solar cells based on HR-3DOM TiO_2 under dark conditions.

Table 2 Resistances of N719 dye-sensitized solar cells based on HR-3DOM TiO_2

Films	R_s/Ω cm^2	Error/%	R_t/Ω cm^2	Error/%	R_{ct}/Ω cm^2	Error/%
Ti-155	6.87	0.76	2.39	3.96	10.97	1.86
Ti-115	6.92	1.23	2.61	5.72	13.72	2.11
Ti-105	7.05	1.04	2.34	5.21	16.17	1.38
Ti-85	7.12	1.36	2.45	5.54	16.55	1.99

capabilities of these DSCs reduced with the decreasing macropore size of hierarchically structured porous TiO_2 in the order of Ti-155 < Ti-115 < Ti-105 < Ti-85, whose changing trends were the same as the open-circuit voltage variations of these DSCs. These results are consistent with the result obtained by the *J–V* test (Fig. 5) and IMVS study (Fig. 7(B)).

3. Conclusions

Herein, a kind of TiO_2 photoanode with hierarchically structured pores filled with nanoparticles was prepared by using hierarchically structured three-dimensionally ordered macroporous (HS-3DOM) TiO_2. In this paper, we reported the synthesis method of HS-3DOM TiO_2 with different macropore sizes (155, 115, 105, and 85 nm) by using well-arrayed PMMA microspheres. The results of their physical characterization showed that micropores and macropores coexisted in all the HS-3DOM TiO_2 samples with an anatase crystal structure. Hierarchically structured porous TiO_2 layers fabricated from HS-3DOM TiO_2 exhibited two kinds of morphologies, including the ones of nanoparticles filled into macropores and the ones of nanoparticles blocked on the surface of macropores. The highest energy conversion efficiency of these devices was achieved at 9.44% for the DSC device based on Ti-105 with the highest short-circuit current density (J_{sc} = 20.76 mA cm^{-2}), which was the main factor influencing the efficiency due to the little change in the open-circuit voltage V_{oc}. The amount of dye adsorption (101.5–114.8 mmol cm^{-2}), which was affected by the surface area, pore volume, and thickness of the photoanode, affected the DSC short-circuit current density and was just in the same sequence of J_{sc} (Ti-85 < Ti-155 < Ti-115 < Ti-105). What's more, the light scattering capability of the photoanode, another important factor influencing the J_{sc}, exhibited the same sequence, too. The IMPS/IMVS results showed that the effective electron transport τ_t and electron lifetime τ_r increased in the order of Ti-155 < Ti-115 < Ti-105 < Ti-85, which was proved by EIS. The efficiencies were also affected by the electron collection efficiency η_{col} which was obtained with τ_t and τ_r.

4. Experimental section

Synthesis of highly ordered PMMA colloidal crystal microspheres

The PMMA colloidal crystal microspheres with different diameters were synthesized using an emulsifier-free emulsion polymerization approach by adjusting the used amount of $K_2S_2O_8$ and MMA.[16] A three-necked round-bottomed alaskite reactor filled with deionized water equipped with a magnetic stirrer was heated at 70 °C. A water-cooling condenser with the upper end connected to a wash-bottle containing ethanol solution was fixed to the reactor. A certain amount of methyl methacrylate monomer was poured into the reactor at 70 °C. After stirring thoroughly with water, $K_2S_2O_8$ as a polymerization inhibitor was added into the reactor under stirring. Then, a milky white solution containing PMMA could be generated after 40 min. The reaction could be stopped by dropwise addition of the solution into cool deionized water. The highly ordered PMMA arrays could be acquired by centrifugation of the PMMA-containing liquid. All of the experimental processes must be protected by a N_2 atmosphere. Herein, PMMA with 280, 220, and 200 nm macropore diameters could be fabricated by using 115 mL of MMA in 1300 mL of water with 0.4, 0.2, and 0.1 g of $K_2S_2O_8$, respectively. PMMA with 150 nm diameter could be obtained by using 30 mL of MMA in 330 mL of water with 0.2 g of $K_2S_2O_8$.

Synthesis of hierarchically structured three-dimensional macroporous TiO_2 pastes

The titanic precursor was tetraisopropyl titanate ($Ti(OC_4H_8)_4$) solution (40 vol%) containing 2 mol L^{-1} concentrate nitric acid and 0.2 mol L^{-1} PEG-400 additives. The total amount of the precursor was 25 mL. The obtained well-arrayed PMMA templates were impregnated into the above precursor solution for 4 hours under room conditions. After filtering the excessive liquid, the obtained samples were dried in a desiccator. Then, the hierarchically structured three-dimensionally ordered macroporous (HS-3DOM) TiO_2 samples could be obtained by calcinating the precursor in air at a ramp of 1 °C min^{-1} from room temperature to 200 °C and 550 °C and kept at these temperatures for 3 h. The macropore size of HS-3DOM TiO_2 depends on the diameter of the PMMA microsphere. Herein, the as-fabricated HS-3DOM TiO_2 samples with a macropore size of *ca.* 155, 115, 105, and 85 nm were fabricated using PMMA microspheres with 280, 220, 200 and 115 nm diameters, respectively, and can be denoted as Ti-155, Ti-115, Ti-105, and Ti-85 according to their macropore sizes. The HS-3DOM TiO_2 pastes could be obtained *via* the following method: add 0.05 g of the as-obtained HS-3DOM TiO_2 powders into 0.4 mL of ethanol solution (50%). The mixtures were sequentially treated by ultrasonic treatment with 60 Hz for 1 min and mixing for 1 min. The resulting pastes could be obtained after 5 cycles.

Assembly of dye-sensitized solar cells

The FTO-coated glass was used as the substrate after washing subsequently with diluted cleaning detergent solution, deionized water, acetone, and ethanol. A liquid admixture containing 1 mL tetraisopropyl titanate, 0.5 mL ethanolamine, and 5 mL ethylene glycol monomethyl ether was spin-coated onto the clean substrates at 3000 rpm. A compact TiO_2 layer was formed after drying at 160 °C for 1 h and sintering at 500 °C for 1 h. It was used to prevent the direct contact between the substrate and the electrolyte. The doctor-blade technique was used to

prepare the porous TiO_2 layer onto the compact layer. After thermal treatment under 125 °C for 1 h and 450 °C for 2 h, the resulting photoanode was immersed in 0.3 mM N719 absolute ethanol solution for 72 h, followed by cleaning with absolute ethanol. The chemically platinized silicon wafer (Co. Ltd. PV-Tech) was used as a counter electrode. The electrolyte (OPV-AN-I, Co. Ltd. PV-Tech) was sandwiched by a sensitized TiO_2 electrode and a counter electrode with two clips.

Characterization

The morphology, crystal structure, and surface area of the as-fabricated HS-3DOM TiO_2 samples were characterized by Scanning Electron Microscopy (SEM, Gemini Zeiss Supra 55), High-Resolution Transmission Electron Microscopy (HR-TEM, JEOL-2010), X-Ray Diffraction (Bruker/AXS D8 Advance), and nitrogen sorption isotherms (Micrometeritic 2020), respectively. Current–voltage behaviors were characterized under simulated AM 1.5 sunlight with an output power of 100 mW cm^{-2}, which was calibrated using a NREL-calibrated Si solar cell, generated using a solar simulator (91192, 1 kW Xe lamp, Oriel). The solar cells were masked with a metal aperture to define an active area of 0.126 ± 0.002 cm^2. A UV-vis-NIR spectrophotometer (Shimadzu, UV-3600) was used to analyze the diffuse reflectance and diffuse transmittance of the TiO_2 films. Intensity-modulated photovoltage spectra (IMPS) at a short circuit and intensity-modulated photocurrent spectra (IMVS) at an open circuit were measured on an electrochemical workstation (Zahner, Zenium) with a frequency response analyzer under blue light emitting diodes (457 nm) driven by a Zahner (PP211) source supply as a modulated light source. Electrochemical impedance spectra (EIS) were measured at an open circuit under dark conditions. Impedance data were fitted using Zview 3.3e software (Scribner Associates, Inc.).

Acknowledgements

This work was supported by the "thousands talents" program for pioneer researcher and his innovation team, China. This work was also supported by the National Science Foundation of China (51374029), Program for New Century Excellent Talents in University (NCET-13-0668), Fundamental Research Funds for the Central Universities (FRF-TP-14-008C1) and China Postdoctoral Science Foundation (2014M550675).

References

1 (*a*) M. Grätzel, *J. Photochem. Photobiol., C*, 2003, **4**, 145; (*b*) Q. Zhang, C. S. Dandeneau, X. Zhou and G. Cao, *Adv. Mater.*, 2009, **21**, 4087; (*c*) Q. Zhang and G. Cao, *Nano Today*, 2011, **6**, 91; (*d*) Q. Zhang, E. Uchaker, S. L. Candelaria and G. Cao, *Chem. Soc. Rev.*, 2013, **42**, 3127.

2 (*a*) S. Mathew, A. Yella, P. Gao, R. Humphry-Baker, B. F. E. Curchod, N. Ashari-Astani, I. Tavernelli, U. Rothlisberger, M. K. Nazeeruddin and M. Graetzel, *Nat. Chem.*, 2014, **6**, 242; (*b*) Q. Wang, S. Ito, M. Graetzel, F. Fabregat-Santiago, I. Mora-Sero, J. Bisquert, T. Bessho and H. Imai, *J. Phys. Chem. B*, 2006, **110**, 25210; (*c*) G. W. Crabtree and N. S. Lewis, *Phys. Today*, 2007, **60**, 37; (*d*) M. Grätzel, *Inorg. Chem.*, 2005, **44**, 6841.

3 (*a*) B. Oregan and M. Grätzel, *Nature*, 1991, **353**, 737; (*b*) D. B. Kuang, S. Ito, B. Wenger, C. Klein, J. E. Moser, R. Humphry-Baker, S. M. Zakeeruddin and M. Grätzel, *J. Am. Chem. Soc.*, 2006, **128**, 4146; (*c*) C. J. Barbe, F. Arendse, P. Comte, M. Jirousek, F. Lenzmann, V. Shklover and M. Grätzel, *J. Am. Ceram. Soc.*, 1997, **80**, 3157.

4 Q. Zhang and G. Cao, *J. Mater. Chem.*, 2011, **21**, 6769.

5 M. Grätzel, *Nature*, 2001, **414**, 338.

6 M. Law, L. E. Greene, J. C. Johnson, R. Saykally and P. D. Yang, *Nat. Mater.*, 2005, **4**, 455.

7 (*a*) Z. Nie, X. Zhou, Q. Zhang, G. Cao and J. Liu, *Sci. Adv. Mater.*, 2013, **5**, 1750; (*b*) R. Gao, Z. Liang, J. Tian, Q. Zhang, L. Wang and G. Cao, in *Fullerenes, Nanotubes, and Carbon Nanostructures – 221st Ecs Meeting*, 2013, p. 127; (*c*) R. Gao, J. Tian, Z. Liang, Q. Zhang, L. Wang and G. Cao, *Nanoscale*, 2013, **5**, 1894; (*d*) J. Lin, A. Nattestad, H. Yu, Y. Bai, L. Wang, S. X. Dou and J. H. Kim, *J. Mater. Chem. A*, 2014, **2**, 8902; (*e*) J. Lin, Y.-U. Heo, A. Nattestad, Z. Sun, L. Wang, J. H. Kim and S. X. Dou, *Sci. Rep.*, 2014, **4**, 5769.

8 K. Park, Q. Zhang, B. B. Garcia and G. Cao, *J. Phys. Chem. C*, 2011, **115**, 4927.

9 J. I. L. Chen, G. von Freymann, V. Kitaev and G. A. Ozin, *J. Am. Chem. Soc.*, 2007, **129**, 1196.

10 (*a*) S. Nishimura, N. Abrams, B. A. Lewis, L. I. Halaoui, T. E. Mallouk, K. D. Benkstein, J. van de Lagemaat and A. J. Frank, *J. Am. Chem. Soc.*, 2003, **125**, 6306; (*b*) L. I. Halaoui, N. M. Abrams and T. E. Mallouk, *J. Phys. Chem. B*, 2005, **109**, 6334; (*c*) I. Rodriguez, F. Ramiro-Manzano, P. Atienzar, J. M. Martinez, F. Meseguer, H. Garcia and A. Corma, *J. Mater. Chem.*, 2007, **17**, 3205.

11 B. T. Holland, C. F. Blanford and A. Stein, *Science*, 1998, **281**, 538.

12 Z. Cai, J. Teng, Z. Xiong, Y. Li, Q. Li, X. Lu and X. S. Zhao, *Langmuir*, 2011, **27**, 5157.

13 J. W. Galusha, C.-K. Tsung, G. D. Stucky and M. H. Bartl, *Chem. Mater.*, 2008, **20**, 4925.

14 H. Jiang, X. Yang, C. Chen, Y. Zhu and C. Li, *New J. Chem.*, 2013, **37**, 1578.

15 (*a*) Z. Y. Zhong, F. X. Chen, T. P. Ang, Y. F. Han, W. Q. Lim and A. Gedanken, *Inorg. Chem.*, 2006, **45**, 4619; (*b*) S. H. Lim, J. Z. Luo, Z. Y. Zhong, W. Ji and J. Y. Lin, *Inorg. Chem.*, 2005, **44**, 4124.

16 H. Li, L. Zhang, H. Dai and H. He, *Inorg. Chem.*, 2009, **48**, 4421.

17 (*a*) S. Bordere, P. L. Llewellyn, F. Rouquerol and J. Rouquerol, *Langmuir*, 1998, **14**, 4217; (*b*) J.-X. Hu, H. Shang, J.-G. Wang, L. Luo, Q. Xiao, Y.-J. Zhong and W.-D. Zhu, *Ind. Eng. Chem. Res.*, 2014, **53**, 11828.

18 H. W. Yan, C. F. Blanford, B. T. Holland, W. H. Smyrl and A. Stein, *Chem. Mater.*, 2000, **12**, 1134.

19 J. Jeromenok and J. Weber, *Langmuir*, 2013, **29**, 12982.

20 Q. Zhang, T. P. Chou, B. Russo, S. A. Jenekhe and G. Cao, *Adv. Funct. Mater.*, 2008, **18**, 1654.

21 C. S. Rustomji, C. J. Frandsen, S. Jin and M. J. Tauber, *J. Phys. Chem. B*, 2010, **114**, 14537.
22 Y. H. Ko, G. S. R. Raju, S. Kim and J. S. Yu, *Phys. Status Solidi A*, 2012, **209**, 2161.
23 (*a*) K. Zhu, N. R. Neale, A. Miedaner and A. J. Frank, *Nano Lett.*, 2007, **7**, 69–74; (*b*) K. Zhu, T. B. Vinzant, N. R. Neale and A. J. Frank, *Nano Lett.*, 2007, **7**, 3739.
24 L.-C. Du and Y.-X. Weng, *J. Phys. Chem. C*, 2007, **111**, 4567.
25 G. Schlichthorl, N. G. Park and A. J. Frank, *J. Phys. Chem. B*, 1999, **103**, 782.
26 K. Zhu, S.-R. Jang and A. J. Frank, *J. Phys. Chem. Lett.*, 2011, **2**, 1070.